Supporting Information

In situ quantitative single-molecule study of site-specific photocatalytic activity and dynamics on ultrathin g-C_3N_4 nanosheets

Shuyang Wu, Jenica Marie L. Madridejos, Jinn-Kye Lee, Yunpeng Lu, Rong Xu, Zhengyang Zhang*

School of Chemistry, Chemical Engineering and Biotechnology, Nanyang Technological University, 21 Nanyang Link, Singapore 637371.

Corresponding Author

E-mail: zhang.zy@ntu.edu.sg

Determine single-molecule catalytic turnovers with nanometer resolution.

Based on **Fig. 5c**, the fluorescence intensity spreads over a few pixels as a point spread function. Briefly, the resolution can be determined using the method reported in the previous work.[1, 2] As shown in **Fig. 5c**, the center position can be localized by fitting the intensity signals with 2D elliptical Gaussian functions (**Eqn. S1**):

$$I(x,y) = A + B * exp(-(\frac{(x-x_0)^2}{2S_x^2} + \frac{(y-y_0)^2}{2S_y^2})) \quad \text{(S1)}$$

where (x_0, y_0) is the center position, A is the background level, B is the peak intensity at (x_0, y_0), S_x and S_y are the standard deviations of the Gaussian distribution along the x- and y-axes, respectively. The localization precision (σ_j, $_{j=x, y}$) can be determined by the pixel size of the camera, the photons collected and background noise level using **Eqn. S2**:

$$\sigma_j = \sqrt{(\frac{S_j^2}{N} + \frac{a^2/12}{N} + \frac{8\pi S_j^4 b^2}{a^2 N^2})} \quad \text{(S2)}$$

where N is the photons collected, a is the pixel size, and b is the background noise in photons. For the fluorescent burst in **Fig. 5c**, the parameters are calculated to be S_x = 158 nm, S_y = 147 nm, a = 160 nm, N = 461 and b = 4. Hence, σ_x =10 nm and σ_y =9 nm are determined. The average localization precision is calculated to be σ_{xy} = 10 nm using **Eqn. S3**:

$$\sigma_{xy} = (\sigma_x + \sigma_y)/2 \quad \text{(S3)}$$

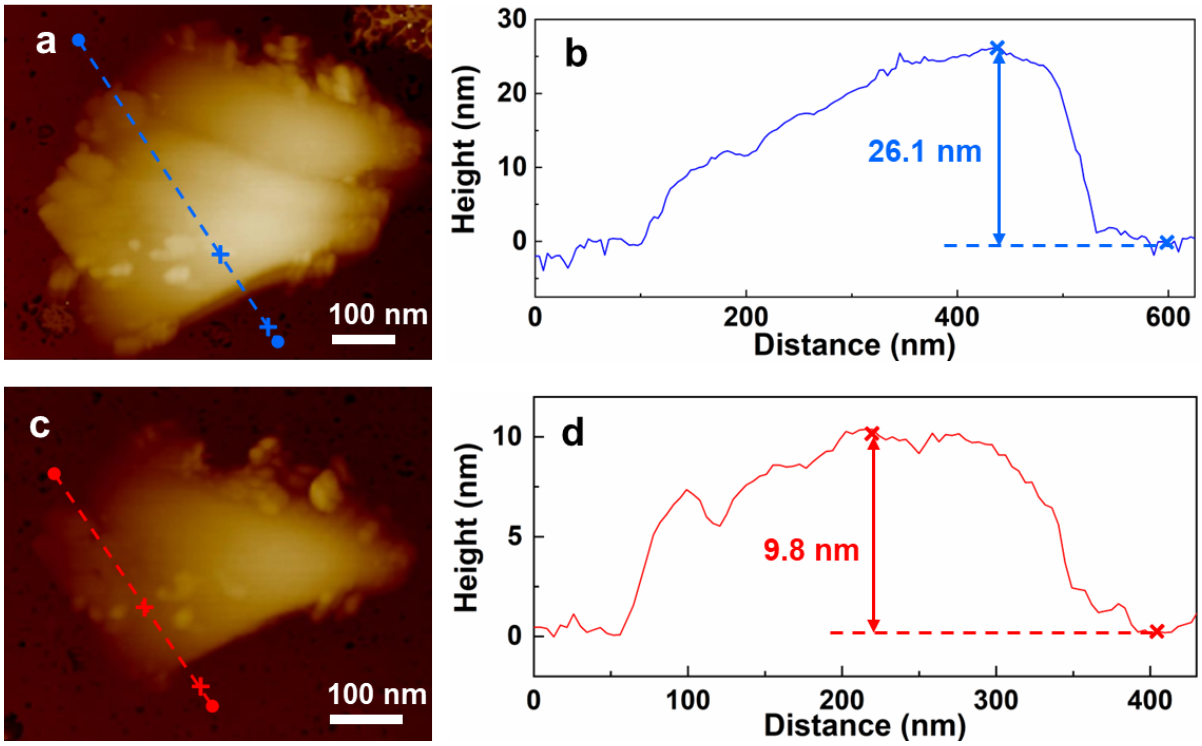

Fig. S1 AFM images and height curves of (a, b) CNS-2 h and (c, d) CNS-6 h.

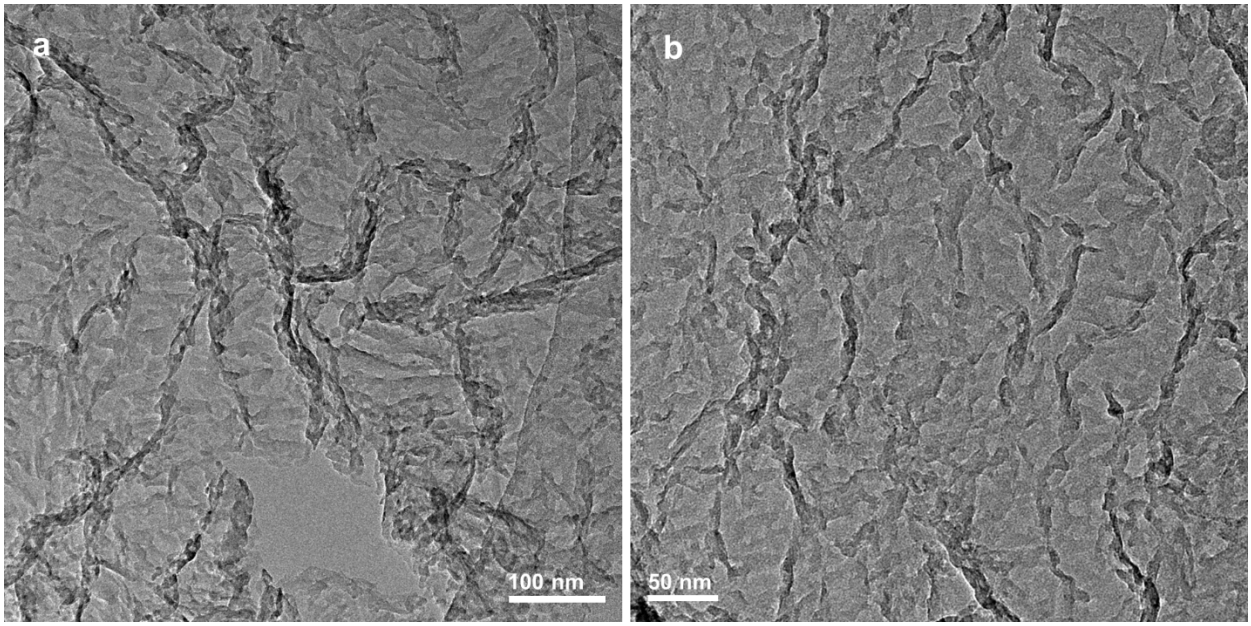

Fig. S2 TEM images of CNS-6 h with wrinkles, edges and basal planes.

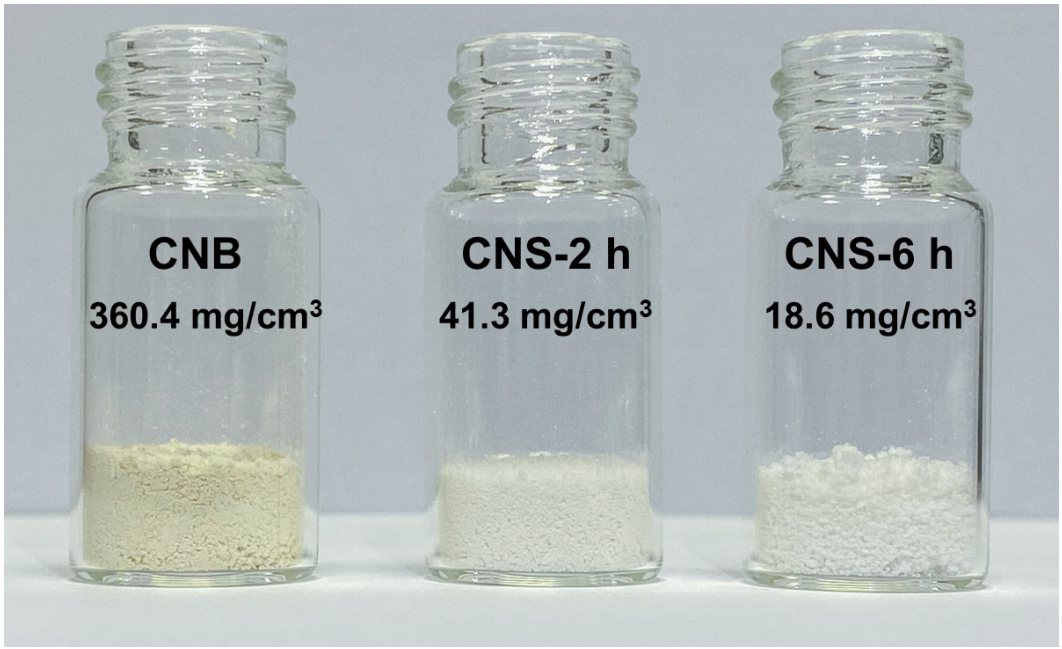

Fig. S3 The comparison of stacking density among as-prepared samples.

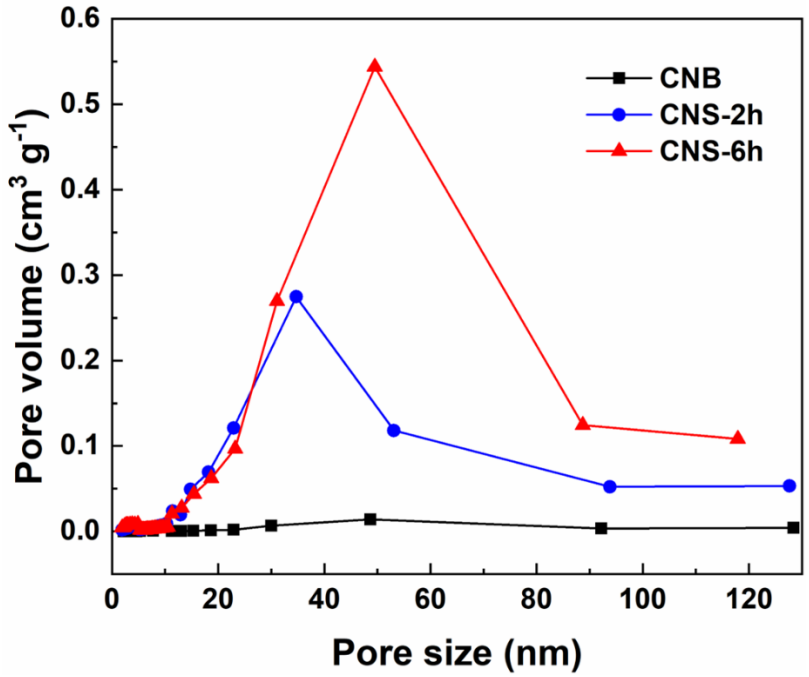

Fig. S4 Pore size distributions of as-prepared samples.

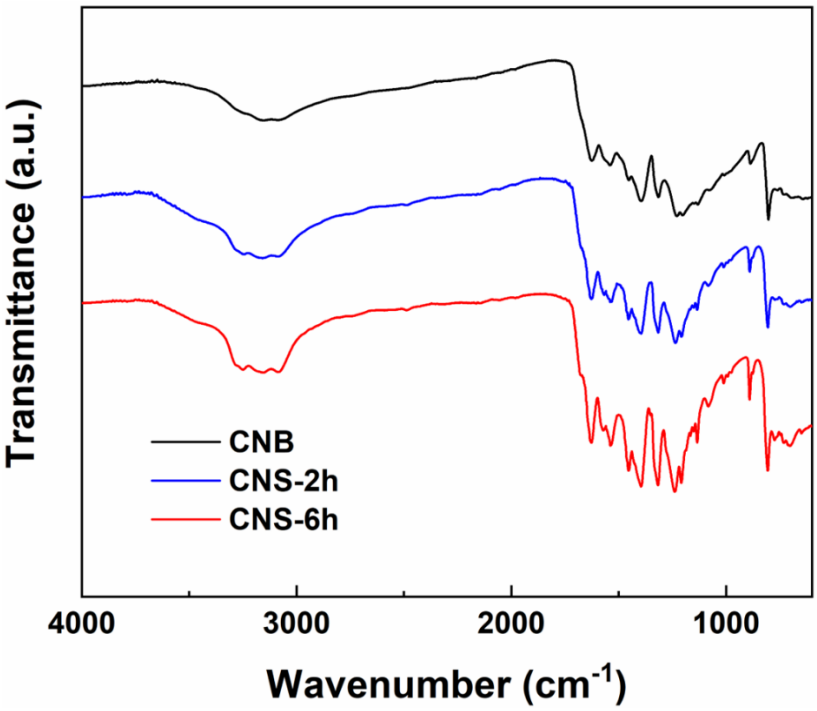

Fig. S5 FTIR spectra of as-prepared samples.

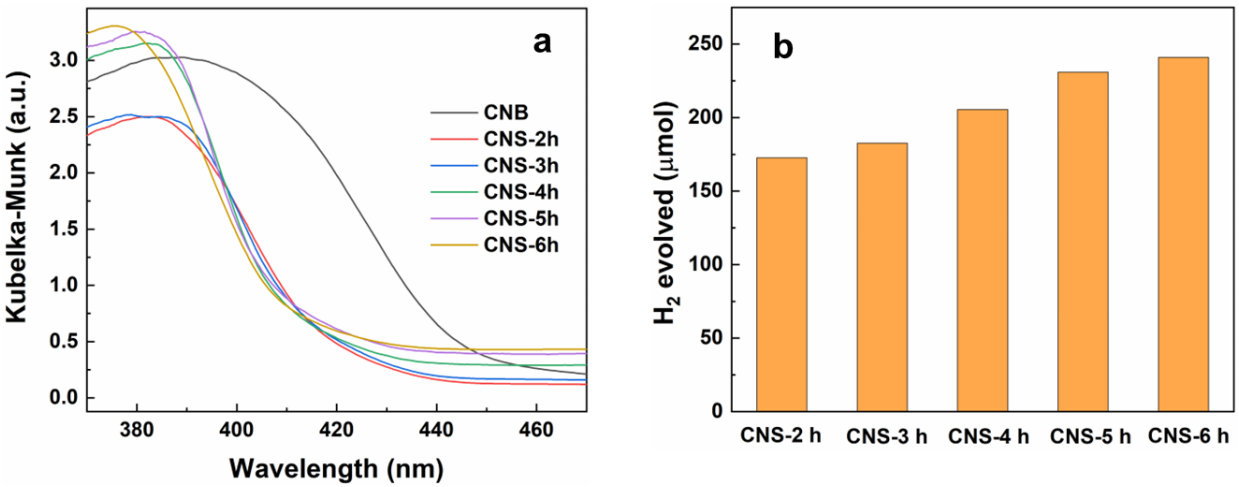

Fig. S6 (a) UV-vis DRS spectra and (b) photocatalytic activity of as-prepared samples (20 mg of photocatalysts, 1 wt% Pt, 15 vol% TEOA, 300 W Xe lamp, > 400 nm, 6 h irradiation).

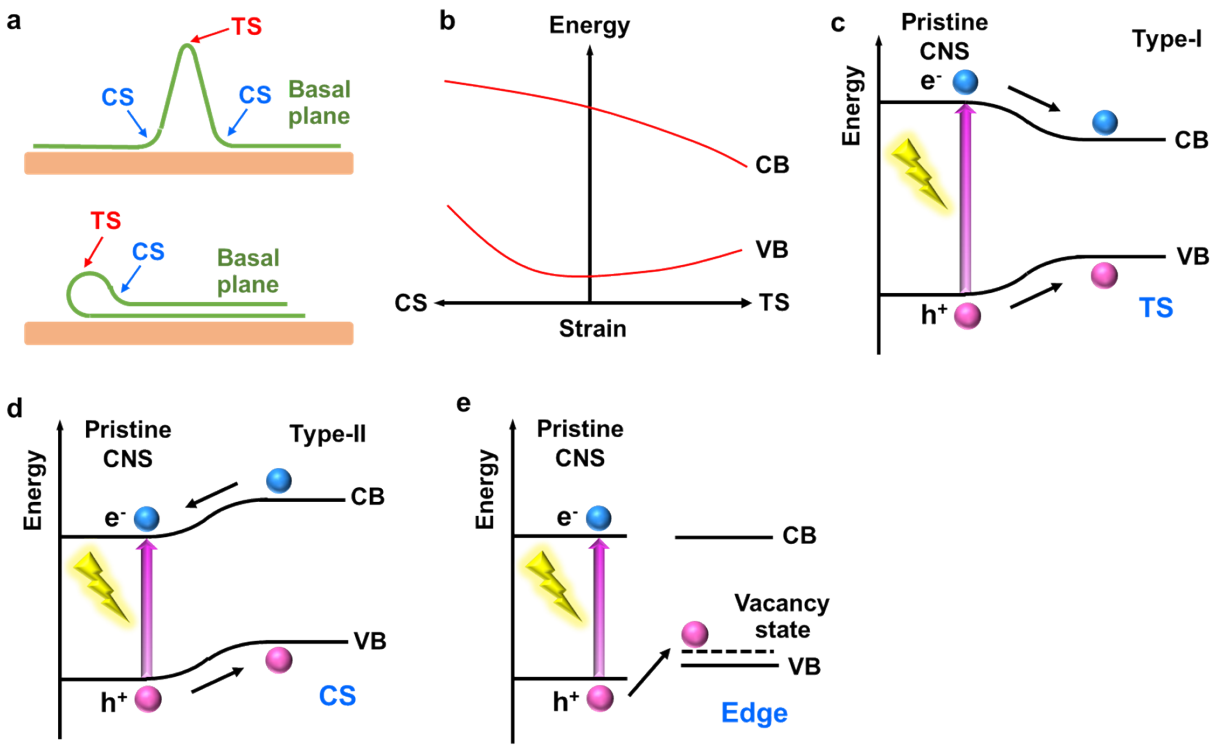

Fig. S7 (a) Strain distributions in the wrinkles. TS and CS represent tensile strain and compressive strain, respectively. (b) The dependence of electronic band positions on the strain present in the structure. Schematic of band alignment between (c) pristine CNS and CNS with tensile wrinkles, (d) pristine CNS and CNS with compressive wrinkles and (e) pristine CNS and CNS with edge vacancies.

Image segmentation.

Image segmentation was conducted before determining the catalytic activities and kinetics of each structure of g-C_3N_4. Generally, the size of the reaction unit (area) can be determined by the intensity-position profile.[1] **Fig. S8b** and **S8c** are the cross-profiles on the wrinkle and edge, respectively, which are marked in the rectangles in **Fig. S8a**. The profiles are fitted by the Gaussian function to obtain the FWHM. As shown in **Fig. S8b** and **S8c**, the FWHM for the wrinkle and edge are calculated to be 346 nm and 318 nm, which are close to the size of two pixels (320 nm). Hence, the edge and wrinkle are dissected into numerous subregions of 2×2 pixels (320 nm × 320 nm). We make sure one fluorescent burst is in each subregion. Otherwise, the size of the subregion is reduced to meet this requirement. For basal planes, we also dissect it into several subregions of 320 nm × 320 nm for convenience with one fluorescent burst in each region.

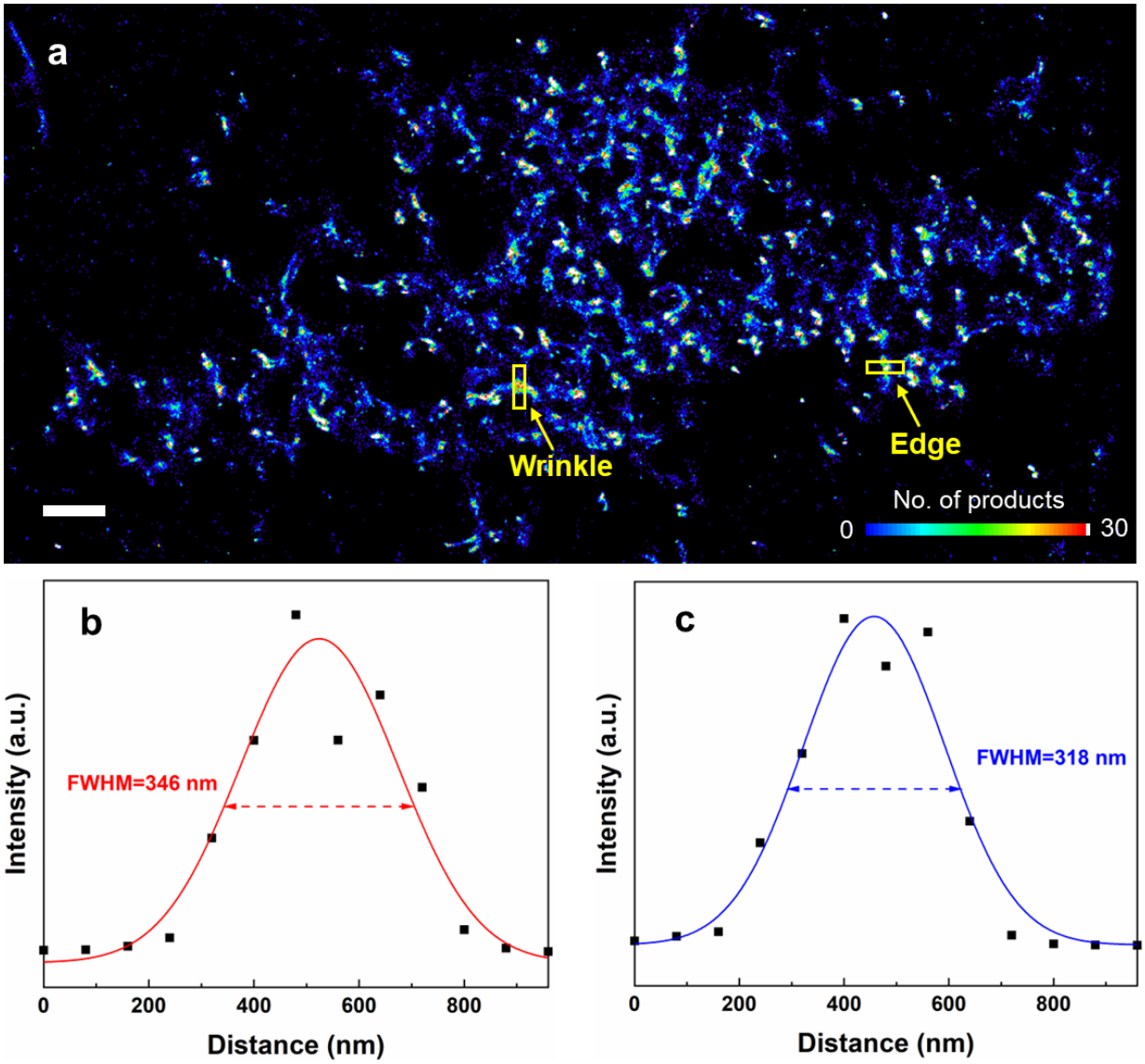

Fig. S8 (a) Image segmentation of wrinkles and edges in the density map. Cross-profile plots of fluorescence intensity at the (b) wrinkle and (c) edge marked in (a).

Resazurin and resorufin adsorption on basal planes, edges and wrinkles by DFT simulation

In the figures below, the initial and corresponding optimized geometries of resazurin and resorufin on different surfaces of g-C_3N_4 are presented in **Fig. S9-S13**. The initial position of adsorbed species on the surfaces affect the final adsorption geometries as well as the energies, thus we started with nine (ten for edge) initial positions to try to cover the most plausible interactions of resazurin and resorufin molecules on the surfaces. It has been previously reported that corrugation in the wrinkle sites of g-C_3N_4 weakens the π delocalization over triazine moeties; however, the structure is still more thermodynamically favored as the sinusoidal-like shape minimizes the electron repulsions of the lone pairs of the nitrogen atoms.[3]

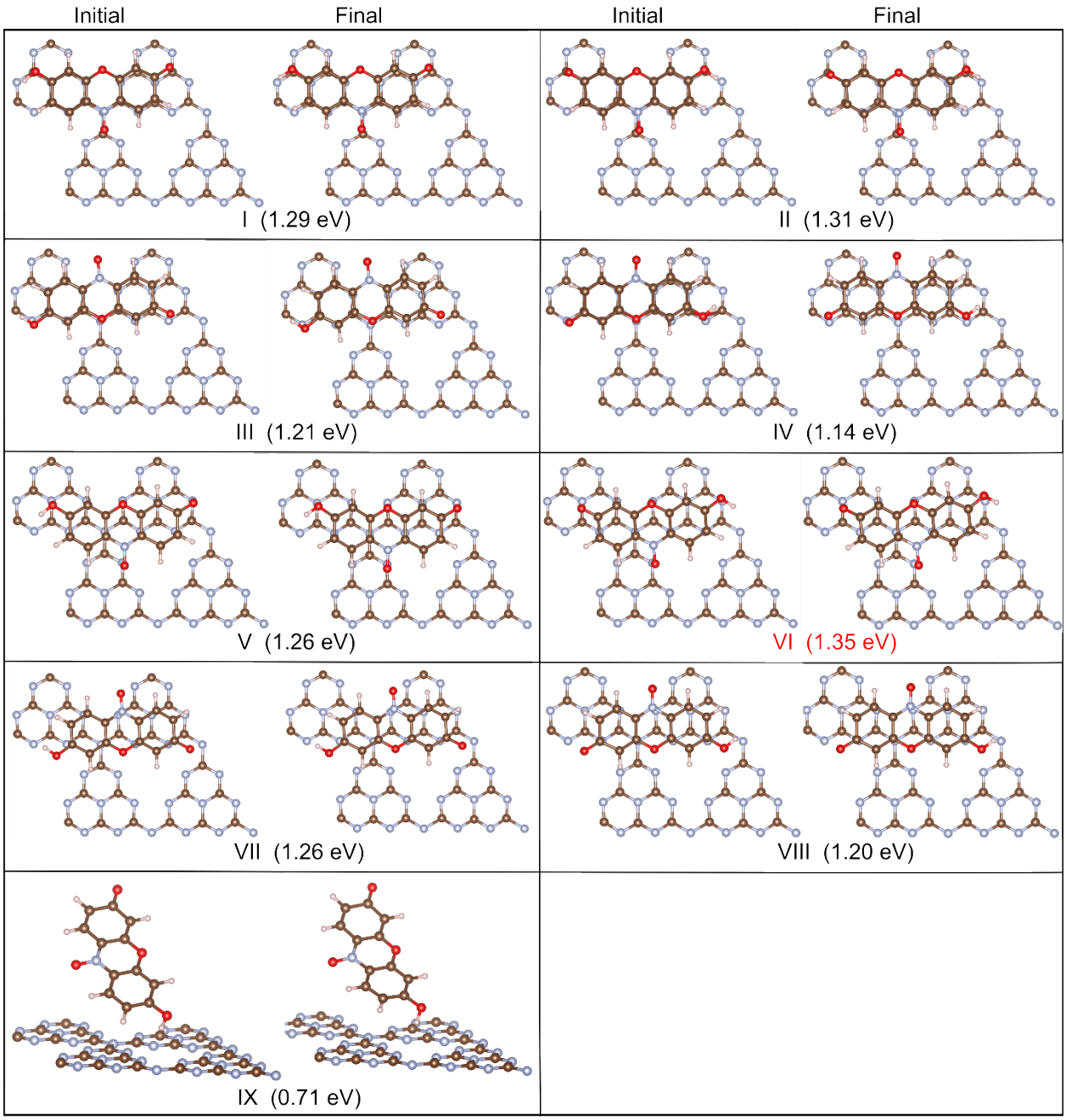

Fig. S9 Initial (left) and optimized (right) geometries of resazurin on the basal plane surface. Structures I-VIII are flat-on configurations while structure IX is an edge-on configuration. The most stable structure (VI) was taken as the final adsorption geometry of resazurin on basal plane surface as reported in **Fig. 7a** of the manuscript.

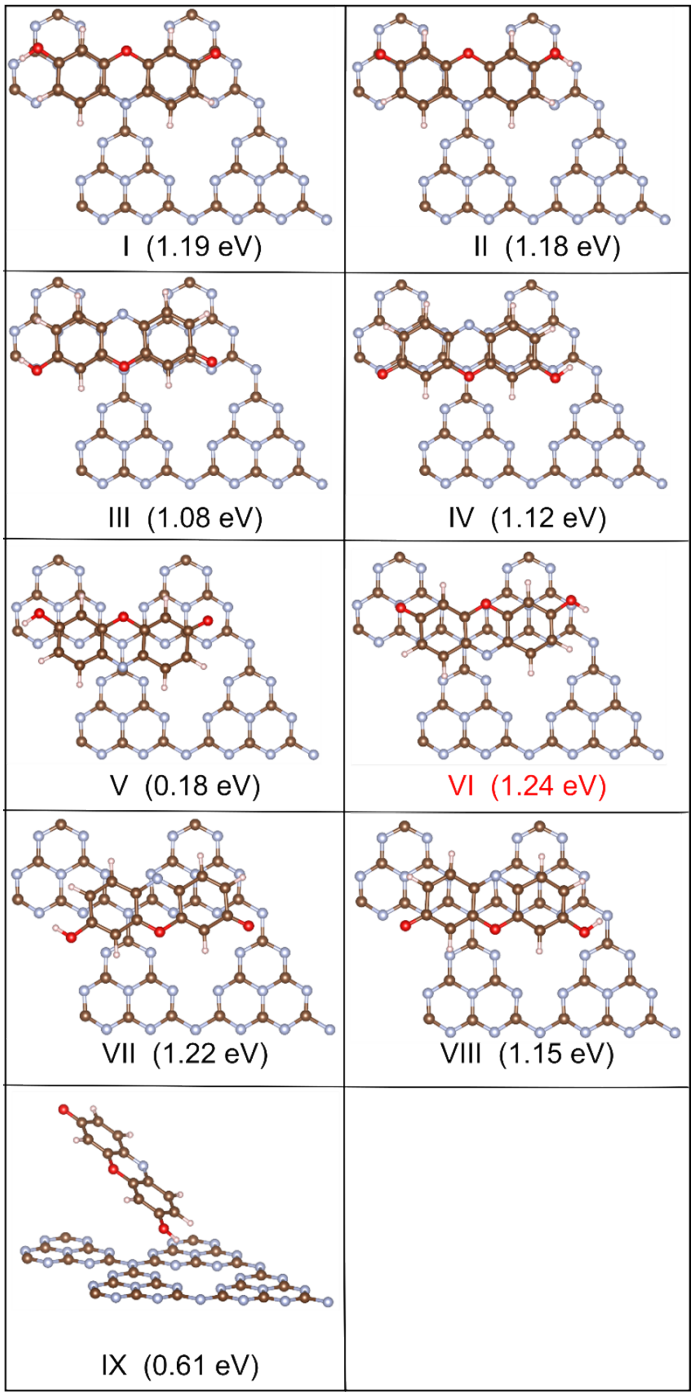

Fig. S10 Optimized geometries of resorufin on the basal plane surface. Structures I-VIII are flat-on configurations while structure IX is an edge-on configuration. The most stable structure (VI) was taken as the final adsorption geometry of resorufin on basal plane surface as reported in **Fig. 7d** of the manuscript.

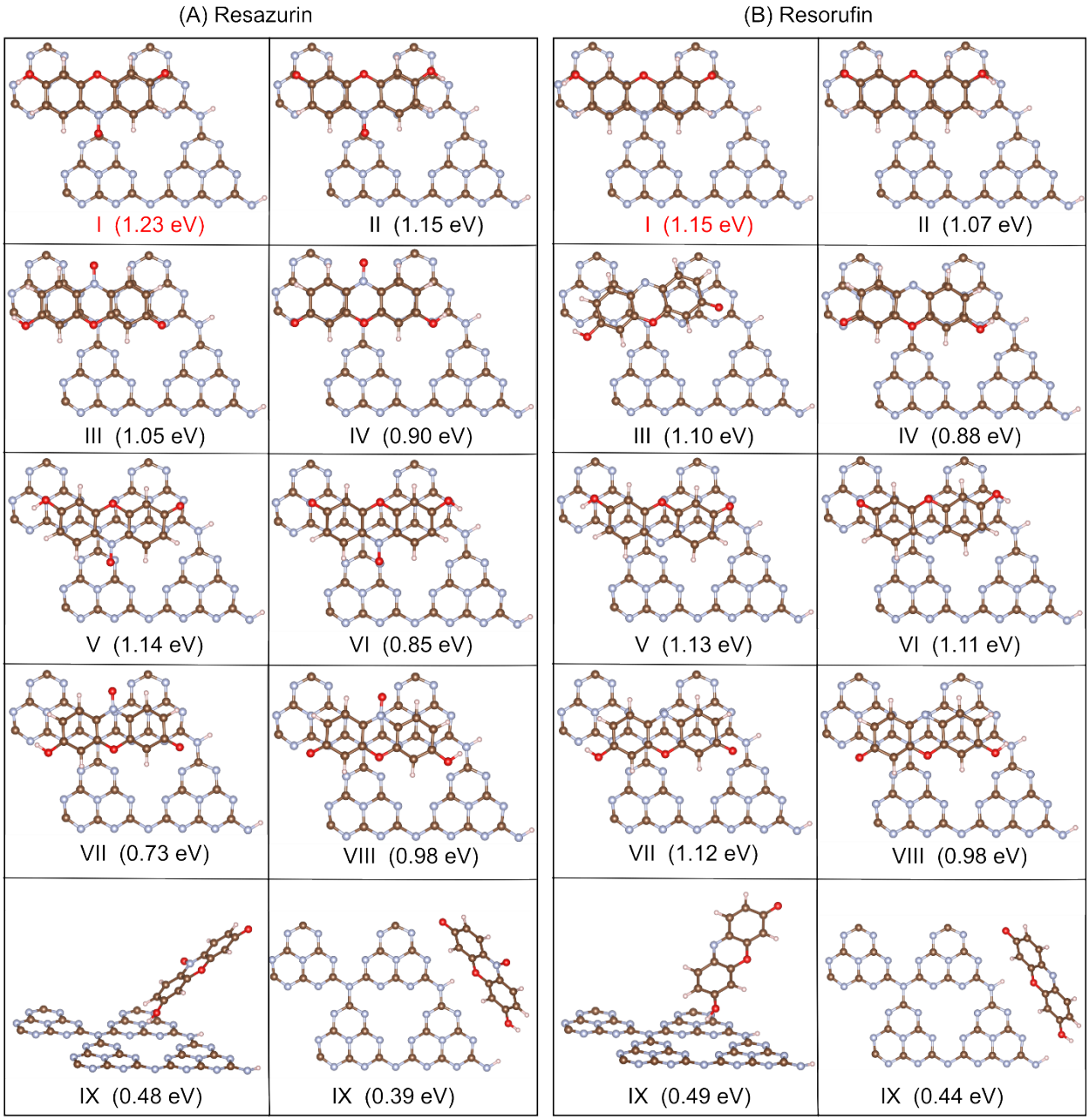

Fig. S11 Optimized geometries of (A) resazurin and (B) resorufin on the edge surface. Structures I-VIII are flat-on configurations while structure IX is an edge-on configuration and X as side configuration. The most stable structures (I) were taken as the final adsorption geometry of resazurin and resorufin on edge surface as reported in **Fig. 7b** and **7e** of the manuscript.

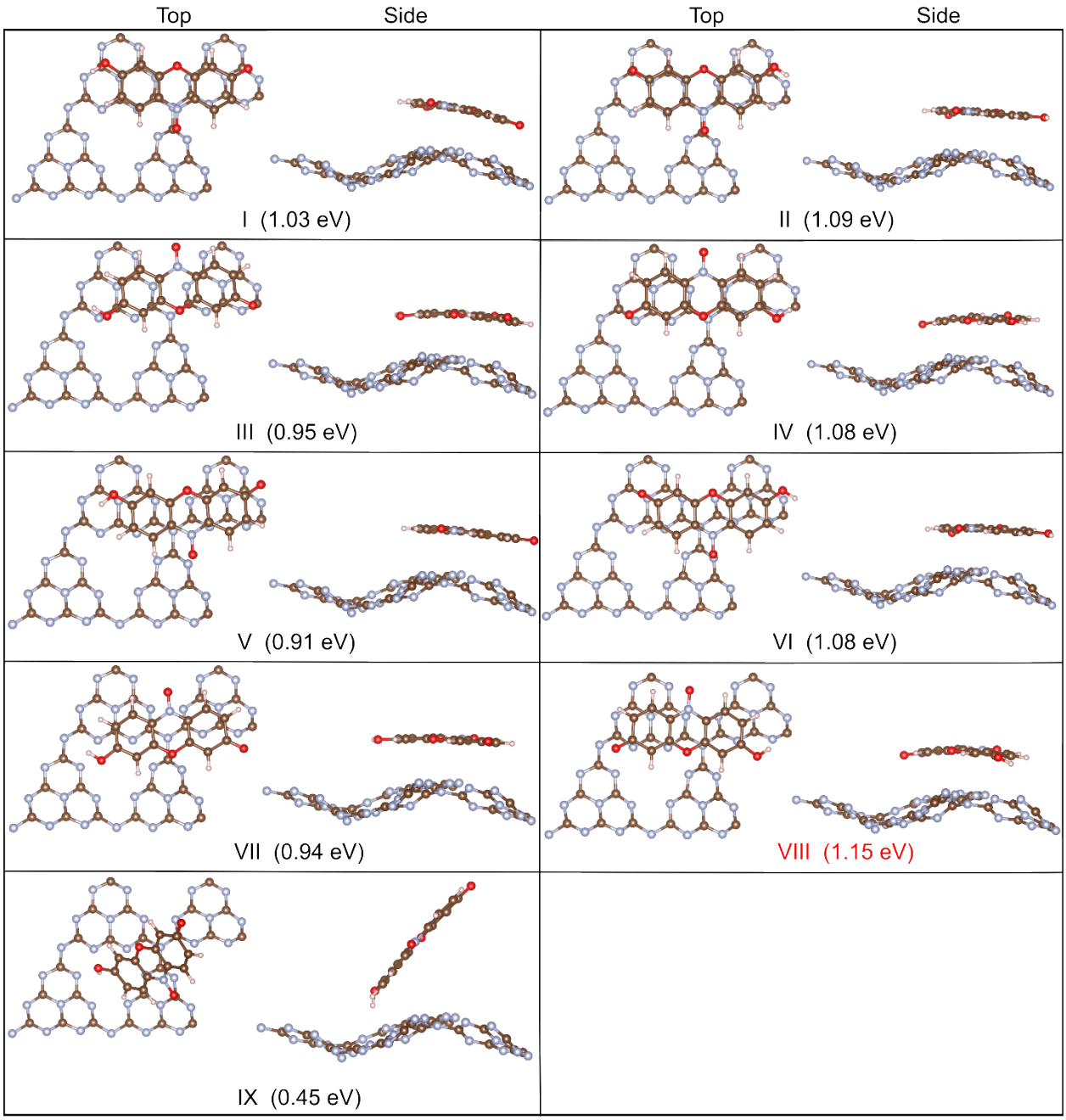

Fig. S12 Optimized geometries of resazurin on the wrinkle surface with top (left) and side (right) views. Structures I-VIII are flat-on configurations while structure IX is an edge-on configuration. The most stable structure (VIII) was taken as the final adsorption geometry of resazurin on basal plane surface as reported in **Fig. 7c** of the manuscript.

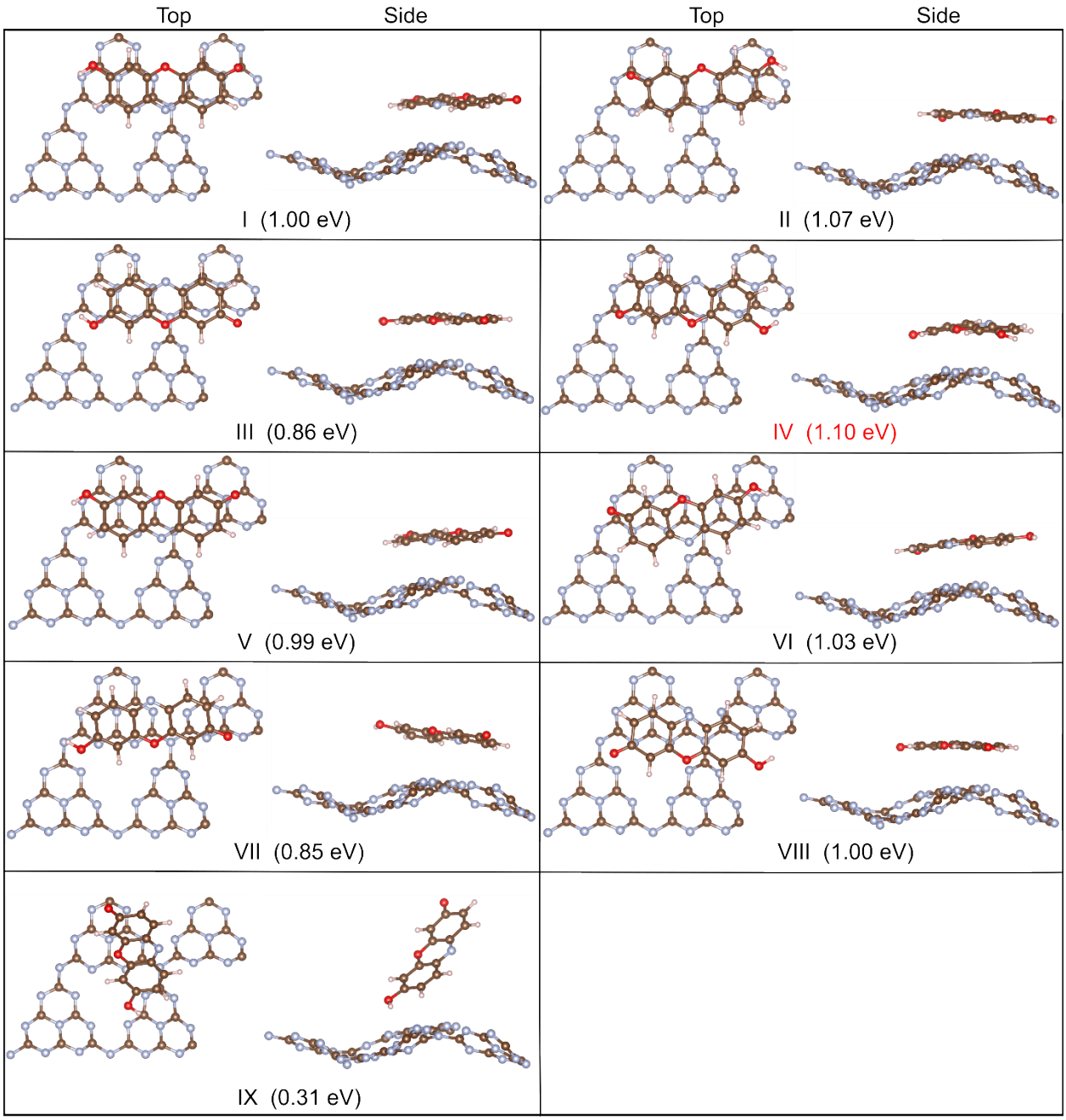

Fig. S13 Optimized geometries of resorufin on the wrinkle surface with top (left) and side (right) views. Structures I-VIII are flat-on configurations while structure IX is an edge-on configuration. The most stable structure (IV) was taken as the final adsorption geometry of resazurin on basal plane surface as reported in **Fig. 7f** of the manuscript.

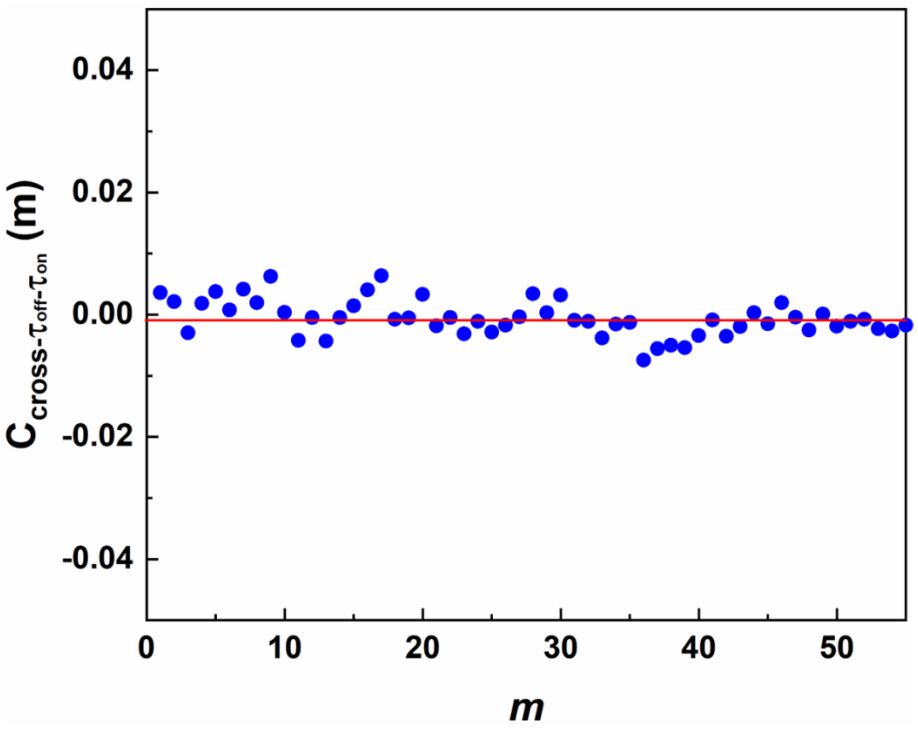

Fig. S14 Cross correlation function of τ_{off} and τ_{on} obtained from the trajectory in **Fig. 8a**.

Table S1. The specific surface area (SSA), pore volume and bandgap energy of as-prepared samples.

Sample	SSA ($m^2 g^{-1}$)	Pore volume ($cm^3 g^{-1}$)	Bandgap energy (eV)
CNB	5.41	0.035	2.85
CNS-2 h	234.27	1.097	3.00
CNS-6 h	307.35	1.330	3.05

Table S2. Summary of g-C_3N_4 catalysts for photocatalytic H_2 generation under visible light.

Ref.	g-C_3N_4 catalysts	Catalyst weight	Light source	Cocatalyst	Scavenger	Activity (μmol h^{-1} g^{-1}), (μmol h^{-1})	AQE (%) (420 nm)
This work	CNS-6 h	20 mg	300 W Xe, > 400 nm	1 wt% Pt	15 vol% TEOA	2008 (40.2)	4.62
[4]	Cyano-group-modified g-C_3N_4	50 mg	420 nm light diodes	1 wt% Pt	10 vol% lactic acid	758.8 (37.9)	1.17
[5]	High-crystalline g-C_3N_4	50 mg	300 W Xe, > 420 nm	3 wt% Pt	10 vol% TEOA	339.4 (17)	3.8
[6]	Nanotubes	25 mg	300 W Xe, > 420 nm	3 wt% Pt	10 vol% TEOA	2100 (52.5)	3.3
[7]	Nanosheets	50 mg	300 W Xe, > 420 nm	3 wt% Pt	10 vol% TEOA	1860 (93)	3.75
[8]	Nanoplatelets	50 mg	300 W Xe, > 420 nm	3 wt% Pt	10 vol% TEOA	1365 (68.3)	3.6
[9]	Mesoporous g-C_3N_4	300 mg	300 W Xe, optical cutoff filters	0.5 wt% Pt	10 vol% TEOA	494 (148.2)	1.8
[10]	Mesoporous g-C_3N_4	100 mg	300 W Xe, > 420 nm	3 wt% Pt	15 vol% TEA	1360 (136)	5.3
[11]	P-doped g-C_3N_4 tubes	100 mg	300 W Xe, > 420 nm	1 wt% Pt	20 vol% methanol	670 (67)	5.7
[12]	Porous g-C_3N_4	25 mg	300 W Xe, > 420 nm	3 wt% Pt	10 vol% TEOA	1300 (32.5)	N/A
[13]	Onion-ring-like g-C_3N_4	10 mg	300 W Xe, > 420 nm	3 wt% Pt	10 vol% TEOA	1900 (19)	N/A
[14]	Multishell nanocapsules	40 mg	300 W Xe, > 420 nm	3 wt% Pt	11 vol% TEOA	630 (25.2)	N/A
[15]	Porous g-C_3N_4	50 mg	300 W Xe, > 420 nm	0.5 wt% Pt	Lactic acid	1216 (60.8)	N/A

Reference

1. T.-X. Huang, B. Dong, S. L. Filbrun, A. A. Okmi, X. Cheng, M. Yang, N. Mansour, S. Lei and N. Fang, *Sci. Adv.*, 2021, **7**, eabj4452.

2. B. Dong, Y. Pei, F. Zhao, T. W. Goh, Z. Qi, C. Xiao, K. Chen, W. Huang and N. Fang, *Nat. Catal.*, 2018, **1**, 135-140.

3. L. M. Azofra, D. R. MacFarlane and C. Sun, *Phys. Chem. Chem. Phys.*, 2016, **18**, 18507-18514.

4. H. Yu, H. Ma, X. Wu, X. Wang, J. Fan and J. Yu, *Sol. RRL*, 2021, **5**, 2000372.

5. L. Wang, Y. Hong, E. Liu, Z. Wang, J. Chen, S. Yang, J. Wang, X. Lin and J. Shi, *Int. J. Hydrog. Energy*, 2020, **45**, 6425-6436.

6. L. Chen, X. Zhao, X. Duan, J. Zhang, Z. Ao, P. Li, S. Wang, Y. Wang, S. Cheng and H. Zhao, *ACS Sustain. Chem. Eng.*, 2020, **8**, 14386-14396.

7. S. Yang, Y. Gong, J. Zhang, L. Zhan, L. Ma, Z. Fang, R. Vajtai, X. Wang and P. M. Ajayan, *Adv. Mater.*, 2013, **25**, 2452-2456.

8. Q. Han, F. Zhao, C. Hu, L. Lv, Z. Zhang, N. Chen and L. Qu, *Nano Res.*, 2015, **8**, 1718-1728.

9. H. Yan, *ChemComm*, 2012, **48**, 3430-3432.

10. J. Hong, X. Xia, Y. Wang and R. Xu, *J. Mater. Chem.*, 2012, **22**, 15006-15012.

11. S. Guo, Z. Deng, M. Li, B. Jiang, C. Tian, Q. Pan and H. Fu, *Angew. Chem.*, 2016, **128**, 1862-1866.

12. Y. Wang, F. He, L. Chen, J. Shang, J. Wang, S. Wang, H. Song, J. Zhang, C. Zhao and S. Wang, *Chin Chem Lett*, 2020, **31**, 2668-2672.

13. L. Cui, J. Song, A. F. McGuire, S. Kang, X. Fang, J. Wang, C. Yin, X. Li, Y. Wang and B. Cui, *ACS Nano*, 2018, **12**, 5551-5558.

14. Z. Tong, D. Yang, Z. Li, Y. Nan, F. Ding, Y. Shen and Z. Jiang, *ACS Nano*, 2017, **11**, 1103-1112.

15. C. Liu, Y. Zhang, F. Dong, X. Du and H. Huang, *J. Phys. Chem. C*, 2016, **120**, 10381-10389.